Inertial migration of a deformable particle in pipe flow

Dhiya Alghalibi,[1,2] Marco E. Rosti,[1,*] and Luca Brandt[1]
[1]*Linné Flow Centre and SeRC (Swedish e-Science Research Centre), KTH Mechanics, S-100 44 Stockholm, Sweden*
[2]*College of Engineering, University of Kufa, Al Najaf, Iraq*

(Received 5 February 2019; published 10 October 2019)

We perform fully Eulerian numerical simulations of an initially spherical hyperelastic particle suspended in a Newtonian pressure-driven flow in a cylindrical straight pipe. We study the full particle migration and deformation for different Reynolds numbers and for various levels of particle elasticity, to disentangle the interplay of inertia and elasticity on the particle focusing. We observe that the particle deforms and undergoes a lateral displacement while traveling downstream through the pipe, finally focusing at the pipe centerline. We note that the migration dynamics and the final equilibrium position are almost independent of the Reynolds number, while they strongly depend on the particle elasticity; in particular, the migration is faster as the elasticity increases (i.e., the particle is more deformable), with the particle reaching the final equilibrium position at the centerline in shorter times. Our simulations show that the results are not affected by the particle initial conditions, position, and velocity. Finally, we explain the particle migration by computing the total force acting on the particle and its different components, viscous and elastic.

DOI: 10.1103/PhysRevFluids.4.104201

I. INTRODUCTION

Particle (a general term to represent beads, capsules, vesicles, red blood cells, etc.) migration in pipe and channel flows of different kind of fluids, Newtonian and non-Newtonian, has been extensively studied because of its importance in many industrial, environmental, and biomedical applications. In these applications, the flow field and the dynamics of the particles' motion are controlled by many parameters, such as the flow conditions, the carrier fluid, wall effects, inertial effects, and particle deformability. The interplay between these various effects results in different interesting phenomena, such as particle separation [1–3] and focusing [4–8]. These phenomena have been successfully applied for the manipulation of particles and cells in microfluidic devices. In this study, we employ a fully Eulerian numerical algorithm based on the one-continuum formulation to fully resolve the fluid-structure interactions and the stresses in the liquid and solid phases and to provide an accurate understanding of the mutual effects of the inertia and particle elasticity on the motion of a deformable particle in a pipe flow, in conditions of interest for inertial microfluidic devices.

In a Newtonian fluid flow, the two most important nondimensional parameters characterizing the deformable particle motion are the Reynolds and Weber numbers, quantifying inertia and particle elasticity, respectively. The Reynolds number Re is defined as the ratio between inertial to viscous effects of the flow, while the ratio of inertia to elastic effects acting on the deformable particle is represented by the Weber number We. Generally, in the absence of inertia (Re $\approx$ 0, i.e., Stokes flow), a neutrally buoyant rigid sphere follows the fluid motion without any lateral migration in order to

*Corresponding author: merosti@mech.kth.se

satisfy the reversibility property of the Stokes flow [9]. On the other hand, deformable particles in the same condition move toward low-shear gradient regions; hence, when suspended in a Poiseuille flow, they migrate toward the center of the channel [10]. The dynamics of deformable particles has mostly been investigated at low Reynolds numbers in the past (see, for example, Refs. [11–15]). Unlike Stokes flow, inertial flows are described by nonlinear governing equations, i.e., the flow system is irreversible. Thus, both rigid and deformable particles trajectories do not necessarily follow the behavior observed in the Stokes regime and particles undergo lateral movement. This is the case for typical inertial microfluidics applications ($\mathrm{Re} > 1$ and $\mathrm{We} > 0$), when inertial and elastic forces dominate the cross-streamline migration and final equilibrium position of the particles. In particular, elastoinertial microfluidics is emerging as a powerful tool and research area, with devices where elasticity and inertia are being engineered to achieve efficient particle focusing and/or particle sorting [16].

Lateral migration and focusing of rigid particles were first observed experimentally in a Newtonian circular pipe flow by Segrè and Silberberg [17]. In a pipe flow, initially randomly distributed neutrally buoyant spheres immersed in a Newtonian carrier fluid migrate radially and focus into a narrow annulus at around 0.6 the pipe radius, resulting in the so-called "tubular pinch" effect. Later on, this effect has been carefully studied in several other analytical [18,19], numerical [20,21], and experimental [22,23] investigations. Recently, an analogous effect was observed in laminar flows in rectangular and square-shaped channels ($1 < \mathrm{Re} < 2300$) [24–26]. Numerous studies which adapted this phenomenon to microfluidics applications described it as "inertial focusing" of particles. Indeed, the equilibrium position of the particles is the net result of two opposing forces resulting from the resistance of the solid particle to the deformation: (i) the shear gradient lift force, which is induced by the velocity profile curve, that directs the particle away from the channel centerline towards the wall and (ii) the wall-induced lift force arising from the interaction of the particle and the neighboring wall that directs the particle away from the wall toward the channel centerline [18,19,27,28]. These two competing forces, determining the lateral trajectory and the final equilibrium position of the particle, are modified differently by the blockage ratio [25] and the flow Reynolds number [23], and thus, by properly designing the geometry of microfluidics device, the lateral motion can be applied and cell focusing, separation, trapping, sorting, enrichment, and filtration achieved (see the review articles by Di Carlo [25] and Karimi *et al.* [2]). Recent simulations from our group reported the mechanism of inertial focusing of both spherical and oblate particles in microfluidics channels, showing the entire migration dynamics of a particle from their initial to final equilibrium position, including particle trajectory, velocity, rotation, and orientation [29].

When the particle is deformable, the dynamics of the particle is further complicated by an additional force called "deformation-induced lift force" arising from the deformation of the particle shape itself that moves the particle toward the centerline and which becomes stronger as the particle deformation increases [30,31]. It is worth noting that the alterations of the particle shape also affect and modify the two forces discussed previously, making the problem fully coupled. During the past 10 years, the dynamics of deformable particles has been studied both numerically [32–36] and experimentally [37,38]. In particular, Hur *et al.* [38] showed that particles can be separated depending on their size and elastic deformability; the same behavior was also observed in numerical simulations [39,40]. In spite of the fact that all the results agree that the soft deformable particles move to the channel centerline, the effect of the flow Reynolds number is not quite understood and still debated. Indeed, while in some cases the final distance of the equilibrium position of the particle from the centerline appears to depend on the flow Reynolds number [41,42], Kilimnik *et al.* [39] found no proof of such a behavior in their numerical simulations. However, they demonstrated that the distance of the final equilibrium position collapses on a single master curve when plotted versus the particles' deformability [43,44].

Most of the previous works on the dynamics of deformable particles in Newtonian flows in cylindrical straight pipes were mainly focused on low-Reynolds-number regimes. In addition, it is challenging to capture in experiments the entire migration dynamics of a deformable particle,

such as its trajectories, the deformed shape, and the forces acting on the particle. Therefore, fully interface-resolved numerical simulations, where the full interactions between the solid and fluid phases are taken into consideration, can became a valuable tool to explore the problem. Also, numerical simulation may provide information about the roles of various control parameters on the particle migration, such as the particle elasticity, the Reynolds number, and the particle initial position.

In this work, we investigate the motion of an hyperelastic deformable particle immersed in a Newtonian Poiseuille flow in a cylindrical straight pipe in different conditions. We focus on the lateral motion of the particle and compare the whole migration dynamics, the trajectory, and the final equilibrium shape of the particle to shed more light onto the particle lateral displacement mechanism and to provide useful knowledge for the design of a microfluidic cylindrical system at finite inertia. In this paper, we investigate the effects of inertia and elasticity on the migration dynamics and equilibrium position of the particle. The paper is organized as follows. In Sec. II, we introduce the governing equations, numerical method, and simulations setup; the results are presented in Sec. III, and finally, the main conclusions and final remarks are summarized in Sec. IV.

II. METHODOLOGY

In this section, we discuss the governing equations, the numerical method used to solve them, and the setup to study the motion of a single deformable viscous hyperelastic particle suspended in a Newtonian pressure-driven Poiseuille flow in a straight cylindrical pipe geometry.

A. Governing equations

In this work, we consider a deformable viscous hyperelastic particle immersed in a Newtonian viscous fluid. Hyperelastic materials show nonlinear stress-strain curves and are generally used to describe gel- and rubber-like substances; for example, Verma and Kumaran [45] found a good agreement between experimental and numerical results where a soft gel is modeled as an incompressible viscous hyperelastic material such as the one used here.

In the present work, both the fluid and solid phases are incompressible and their motion is governed by the momentum conservation equation and the incompressibility constraint

$$\rho\left(\frac{\partial u_i^{\mathrm{f}}}{\partial t}+\frac{\partial u_i^{\mathrm{f}}u_j^{\mathrm{f}}}{\partial x_j}\right)=\frac{\partial \sigma_{ij}^{\mathrm{f}}}{\partial x_j}, \tag{1a}$$

$$\frac{\partial u_i^{\mathrm{f}}}{\partial x_i}=0, \tag{1b}$$

$$\rho\left(\frac{\partial u_i^{\mathrm{s}}}{\partial t}+\frac{\partial u_i^{\mathrm{s}}u_j^{\mathrm{s}}}{\partial x_j}\right)=\frac{\partial \sigma_{ij}^{\mathrm{s}}}{\partial x_j}, \tag{1c}$$

$$\frac{\partial u_i^{\mathrm{s}}}{\partial x_i}=0, \tag{1d}$$

where u, v, and w (u_1, u_2, and u_3) are the velocity streamwise and the two cross-flow components, corresponding to the x, y, and z (x_1, x_2, and x_3) coordinate directions, respectively (see Fig. 1). The superscripts $^{\mathrm{f}}$ and $^{\mathrm{s}}$ in the previous equations are used to distinguish the fluid and solid phases, and σ_{ij} is the Cauchy stress tensor. Note that the density of the fluid and solid phases ρ is equal since we are considering a neutrally buoyant particle. The kinematic and dynamic interactions between the two phases are obtained by imposing the continuity of the velocity (i.e., the no-slip and no-penetration boundary conditions) and of the traction force (i.e., a traction balance) at the interface, i.e.,

$$u_i^{\mathrm{f}}=u_i^{\mathrm{s}}, \tag{2a}$$

$$\sigma_{ij}^{\mathrm{f}}n_j=\sigma_{ij}^{\mathrm{s}}n_j, \tag{2b}$$

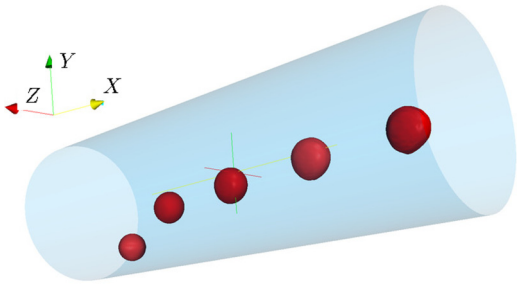

FIG. 1. Visualization of the motion of a single deformable particle, initially spherical with radius r, in a cylindrical straight pipe of radius R, for the case $\mathrm{Re} = 200$ and $\mathrm{We} = 0.5$. The initial radial particle position is at $r = 0.7487R$. The particle and the pipe are shown at the actual scale.

where n_i represents the normal vector at the interface. Finally, we need to define the Cauchy stress tensor for the fluid and solid systems; here, the carrier fluid is assumed to be Newtonian,

$$\sigma_{ij}^{\mathrm{f}} = -P\delta_{ij} + \mu^{\mathrm{f}}\left(\frac{\partial u_i^{\mathrm{f}}}{\partial x_j} + \frac{\partial u_j^{\mathrm{f}}}{\partial x_i}\right), \tag{3}$$

while the particle is an incompressible viscous hyperelastic material experiencing only the isochoric motion with constitutive equation

$$\sigma_{ij}^{\mathrm{s}} = -P\delta_{ij} + \mu^{\mathrm{s}}\left(\frac{\partial u_i^{\mathrm{s}}}{\partial x_j} + \frac{\partial u_j^{\mathrm{s}}}{\partial x_i}\right) + G\xi_{ij}, \tag{4}$$

where δ_{ij} is the Kronecker δ, the pressure is denoted by P, and the dynamic viscosity of the fluid and solid phases are indicated by μ^{f} and μ^{s}, respectively. The last term, $G\xi_{ij}$, is the hyperelastic stress contribution modeled as a neo-Hookean material, where G indicates the modulus of transverse elasticity and ξ_{ij} is the deviatoric left Cauchy-Green deformation tensor (also sometimes called Finger deformation tensor) defined as $\xi = FF^T$, where $F_{ij} = \partial x_i/\partial X_j$ is the deformation gradient (being X and x the initial and current coordinates [46]). The previous set of equations for the solid material can be closed by updating the left Cauchy-Green deformation tensor components with the following transport equation:

$$\frac{\partial \xi_{ij}}{\partial t} + \frac{\partial u_k \xi_{ij}}{\partial x_k} - \xi_{kj}\frac{\partial u_i}{\partial x_k} - \xi_{ik}\frac{\partial u_j}{\partial x_k} = 0; \tag{5}$$

this equation states that the upper convective derivative of ξ is identically equally to zero, which is always true for an hyperelastic material [46].

B. Numerical method

To numerically solve the fluid-structure interaction problem at hand, we employ the so-called one-continuum formulation [47], where only one set of equations is solved over the entire field. This is found by introducing a monolithic velocity vector field, u_i, valid everywhere; this is the weighted average between the values in the two phases, with the weight being a phase indicator function ψ based on the local solid volumetric fraction in each cell [48,49]

$$u_i = (1 - \psi)u_i^{\mathrm{f}} + \psi u_i^{\mathrm{s}}. \tag{6}$$

Thus, $\psi = 0$ or $\psi = 1$ if a computational cell in the domain is located inside the fluid or in the solid phase, while ψ assumes a value between 0 and 1 in the interface cells. Thus, the governing equations (1) can be rewritten as

$$\rho\left(\frac{\partial u_i}{\partial t} + \frac{\partial u_i u_j}{\partial x_j}\right) = \frac{\partial \sigma_{ij}}{\partial x_j}, \tag{7a}$$

$$\frac{\partial u_i}{\partial x_i} = 0, \tag{7b}$$

where the Cauchy stress tensor σ_{ij} is written in a mixture form and defined as

$$\sigma_{ij} = (1 - \psi)\sigma_{ij}^{\mathrm{f}} + \psi\sigma_{ij}^{\mathrm{s}}. \tag{8}$$

Finally, the local solid volume fraction ψ is found by solving an additional transport equation

$$\frac{\partial \psi}{\partial t} + \frac{\partial u_k \psi}{\partial x_k} = 0. \tag{9}$$

We solve Eqs. (7), (5), and (9) in a fully Eulerian formulation on a staggered uniform mesh with velocities located on the cell faces and all the other variables (pressure, fluid, and solid stress components) at the cell centers, as first proposed by Ref. [50]. The time integration is based on an explicit fractional-step method [51], where only the solid hyperelastic contribution in Eq. (1) is advanced with the Crank-Nicolson scheme, while all the other terms are advanced with the third-order Runge-Kutta scheme [52]. All the spatial derivatives are approximated with the second-order centered finite-differences scheme, except for the advection term in Eqs. (5) and (9) where the fifth-order weighted essentially nonoscillatory scheme is applied [50,53,54]. A comprehensive review on the effect of different discretization schemes for the advection terms was studied in Ref. [52]. The pressure is computed by solving the Poisson equation using fast Fourier transforms. In summary, the set of governing equations are solved as follows (see Ref. [55]): (i) the left Cauchy-Green deformation tensor ξ_{ij} and the local solid volume fraction ψ are updated first by solving Eqs. (5) and (9) (update step); (ii) the conservation of momentum equation (7) are advanced in time by first solving the momentum equation (prediction step), then by solving a Poisson equation for the projection variable, and finally by correcting the pressure and velocity to ensure that the velocity field is divergence free (correction step).

The accuracy and validity of the code has been extensively examined in previous works, and more details on the numerical scheme and validation campaign are reported in Refs. [55–57], where very good agreement with literature results is obtained for various test cases. In addition, for more details on the numerical method, the reader is referred to Ref. [50].

C. Simulations setup

In this study, the pressure-driven motion of a hyperelastic deformable particle is examined in a circular straight pipe. The numerical domain is a square duct where the periodic boundary condition is applied in the streamwise x direction, as shown in Fig. 1; the square duct is converted into a pipe via a volume penalization technique [58] that enforces the no-slip and no-penetration boundary conditions on the inner surface of the pipe. The pipe of diameter D is $6D$ long and is discretized with a mesh of 720 grid points in the streamwise direction and 240 grid points in the two cross-flow directions. The immersed particle is initially spherical with an initial diameter d equal to $d = D/5$ (blockage ratio $d/D = 0.2$), which corresponds to 48 Eulerian grid points per particle diameter ($\Delta x_i = 1/48$). We also performed a simulation with a finer mesh of 72 points per particle diameter ($\Delta x_i = 1/72$) and found no appreciable difference, which ensures the grid independence of the results on the coarser grid resolution which is used for all the other cases. In all our simulations, the time-step is chosen to ensure a CFL number equal to 0.2. The present simulations, with a resolution of 48 points per diameter, require approximately 4 to 16 days with 400 computational cores to reach the particle final equilibrium position, depending on the value of the elastic modulus G.

TABLE I. Summary of all the simulations performed in the present study.

Re	100	200	400	r/R	μ^s/μ^f
We	0.125	0.125	0.125	0.2828	1.0
			0.250	0.2828	1.0
	0.500	0.500	0.500	0.2828	1.0
			1.000	0.2828	1.0
			2.000	0.2828	1.0
	4.000	4.000	4.000	0.2828	1.0
			1.000	0.7487	1.0
			1.000	0.0544	1.0
			4.000	0.2828	0.3
			4.000	0.2828	3.0

The problem at hand is defined by two nondimensional parameters: the Reynolds and the Weber numbers. The former is defined as $\mathrm{Re} = \rho D U_b/\mu^f$, where U_b is the bulk velocity across the domain. In our simulations, U_b is kept constant, ensuring a constant mass flux, by applying a varying pressure gradient driving the flow through the domain. We vary the Reynolds number between 100 and 400 to study the inertial migration of the particle in a range of Reynolds number of interest for emerging inertial microfluidics applications [59]. The Weber number is defined as $\mathrm{We} = \rho U_b^2/G$ and is varied between 0.125 and 4, ranging from an almost rigid particle ($\mathrm{We} = 0.125$) to an highly deformable one ($\mathrm{We} = 4$). Two additional nondimensional parameters are the density and viscosity ratios which are fixed equal to 1 in all our simulations. Finally, the particle is initially positioned at a distance $r \approx 0.3R$ from the center of the pipe (where r denotes the radial position of the particle center), except in two additional simulations where the particle is initially located at $r \approx 0.75R$ and $r \approx 0.05R$ to study the effect of the initial position on the results. The full set of simulations and parameters considered in the present study is summarized in Table I.

III. RESULTS

Here, we study the migration of an initially spherical hyperelastic particle in a Hagen-Poiseuille flow of a Newtonian fluid for different Reynolds and Weber numbers and for various solid to fluid viscosity ratios. Figure 1 shows the particle migration for the case $\mathrm{Re} = 400$ and $\mathrm{We} = 1$; we observe that the particle deforms and undergoes a lateral displacement while traveling downstream through the pipe, finally focusing at the pipe centerline, in agreement with previous observations [60]. The same general behavior is found for all the other cases we have investigated, with the full migration process and the final particle equilibrium position being determined by the interplay between the different opposing forces acting on the particle.

The time history of the particle radial position, r, measured from the center of the pipe, is illustrated in Fig. 2 for different Reynolds and Weber numbers. All the particles are released from the same initial position, $r = 0.2828R$, and then migrate toward the center of the pipe, where they settle and reach their equilibrium position on the symmetry axis ($r \approx 0$). In the figure, we can also observe that the particle first displaces from its initial position toward the wall, and only after some time ($tU_b/D \geqslant 10$) starts migrating toward the pipe center. The first outer displacement is caused by the fact that the particle initial shape is spherical, and according to the famous Segrè-Silberberg effects [17], rigid spherical particles tend to migrate toward the walls and settle down at a distance of approximately $r \approx 0.6R$. This equilibrium position originates from the balance of the force coming from the mean shear of the velocity profile pulling the particle towards the wall and the pressure pushing it toward the center. However, after some time the particle deforms and starts displacing toward the pipe center, where it will settle due to the local zero shear rate of the mean velocity profile. The time needed to the particle to invert its motion from the motion toward the wall to the

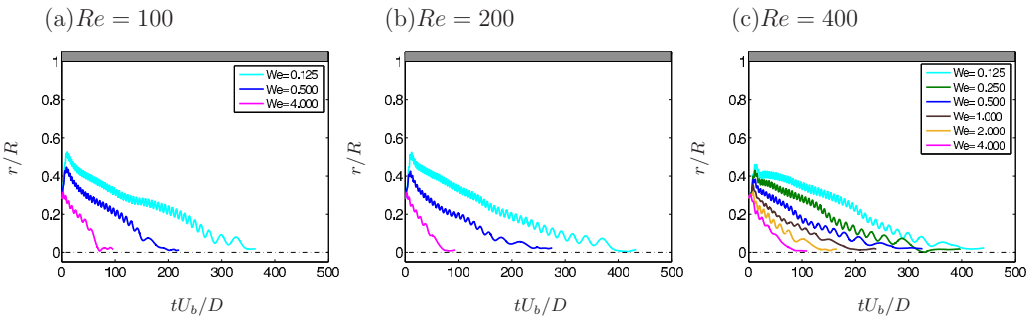

FIG. 2. The time history of the particle radial position r at different Weber numbers We for various Reynolds numbers Re, as indicated in the legend. The radial position r is normalized by the radius of the pipe R whereas time is scaled by D/U_b.

one towards the center decreases with the Weber number, i.e., for high We the particle deformation is fast and the spherical shape is lost within a short time. Finally, from Fig. 2 we can notice that for all the Reynolds number considered, as the Weber number increases, the whole migration process is faster and the final equilibrium position is reached in a shorter time than for the rigid particles cases with low We.

Next, we investigate the effect of the Reynolds number on the dynamics and equilibrium position of the particle at fixed Weber numbers. We show the time history of the particle motion from its initial radial location ($r/R = 0.2828$) to the final equilibrium position ($r/R \simeq 0$) for different Reynolds numbers in Figs. 3(a)–3(c) at three different Weber numbers, We $= 0.125$, 0.5, and 4. Our results clearly show that both the migration dynamics and the final equilibrium position of a deformable particle is almost independent of the Reynolds number, at least in the range considered here (i.e., $100 \leqslant \mathrm{Re} \leqslant 400$), thus suggesting that the dynamics of deformable particles is mainly controlled by the value of the particle elastic modulus G.

To further understand the effect of the Reynolds Re and Weber We numbers on the dynamics of the deformable particle, we measure the time needed for the particle to reach its final focal position, t_{cen}, for all the cases studied. Figure 4 shows the normalized time to equilibrium t_{cen} as a function of the Reynolds number Re [Fig. 4(a)] and of the Weber number We [Fig. 4(b)]. The figure confirms our previous observations that the equilibrium time is strongly affected by We and weakly by Re. In particular, t_{cen} slightly increases with the Reynolds number Re while substantially decreasing with the Weber number We (for example, at Re $= 200$, t_{cen} reduces by almost eight times when increasing We from 0.125 to 4). Finally, in the inset of Fig. 4(b), we report all our data for the case at Re $= 400$, which show that the decay of t_{cen} with We is smooth and monotonic.

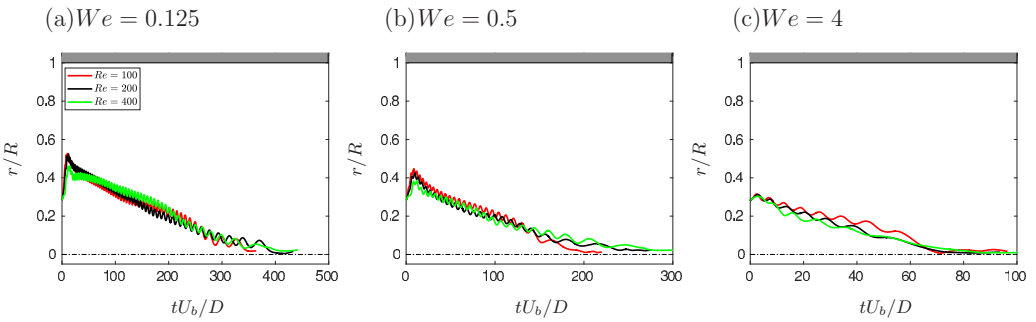

FIG. 3. The time history of the particle radial position r at different Reynolds numbers Re for various Weber numbers We, as indicated in the legend.

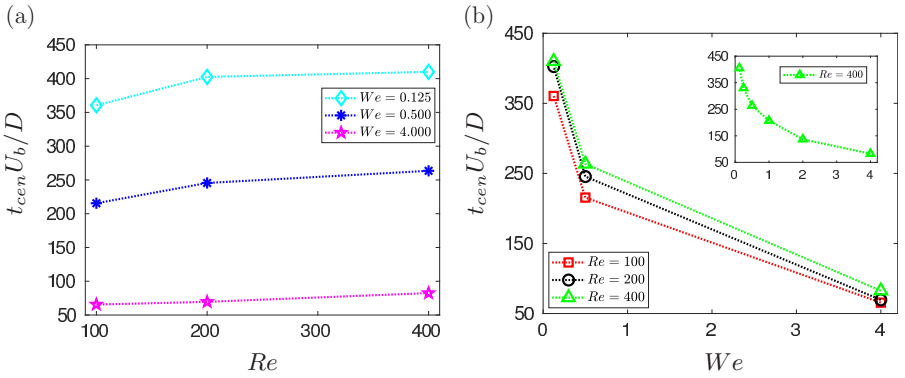

FIG. 4. Normalized time t_{cen} needed to reach the final equilibrium position vs (a) the bulk Reynolds number Re for different We and (b) the Weber number We for different Re.

In both Figs. 2 and 3, we can observe that the particle migration toward the center presents oscillations. Also, the period of the particle oscillations is approximately the same for the different Re at constant We (Fig. 3), while the period increases when increasing the Weber number (Fig. 2), thus suggesting that the oscillations are due to elastic effects only. Figure 5 reports the normalized period of the oscillation, $T_{\text{osc}}U_b/D$, as a function of the Weber number We; T_{osc} is the mean period of the oscillation averaged over the first half of the particle migration process, where the period remains approximately constant, while the second half is neglected since T_{osc} slightly changes and increases when the particle approaches the final equilibrium position. As shown in Fig. 5, the period T_{osc} monotonically and nonlinearly increases with We; in particular, the growth of T_{osc} is very fast for low We, eventually almost saturating at higher We. Also, from the figure we observe that T_{osc} slightly increases with the Reynolds number, although the growth is small compared to the one due to the Weber number We.

The previous results are general and do not depend on the particle initial position and velocity. We show this by examining the effect of the radial initial position and velocity on the dynamics and final equilibrium position of the particle at a fixed Reynolds and Weber numbers. Figure 6(a) shows the time evolution of the radial position of a particle released from three different radial positions

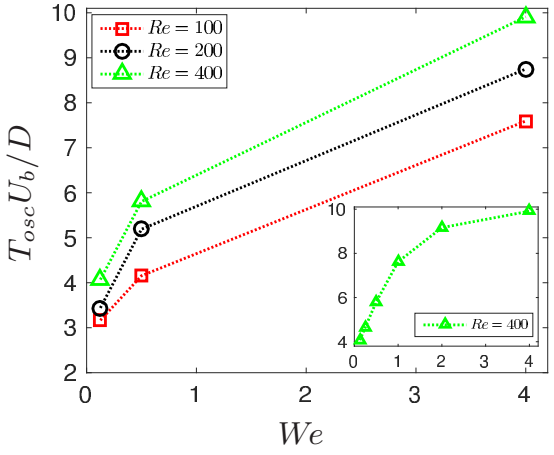

FIG. 5. Normalized period of the particle oscillatory motion, $T_{\text{osc}}U_b/D$, as a function of the Weber number We for different Re.

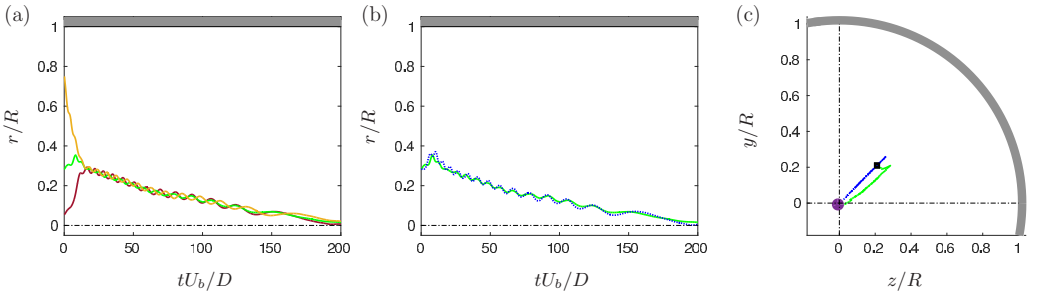

FIG. 6. The time history of the radial position of the deformable particle released at (a) three different initial positions and (b) with two different initial velocities at the same Reynolds and Weber numbers: Re = 400 and We = 1. (c) Trajectory of the particle in the pipe cross section (y-z plane) for the cases reported in panel (b).

($r/R = 0.0544, 0.2828, 0.7487$) at Re = 400 and We = 1. The figure clearly shows that the particle always migrates toward the center of the pipe, independent of its initial radial position. Interestingly, after short initial transients during which the single particles reach the radial position $r \approx 0.29R$, the trajectories collapse into a single oscillating curve for $tU_b/D \gtrsim 15$. Figure 6(b) reports the time evolution of the radial position of a particle released from $r/R = 0.2828$ with two different initial conditions: the solid green line shows the case with the particle released stationary in a fully developed pipe flow (a Poiseuille velocity profile), while the blue dashed line the case where both the particle and fluid are released at rest, i.e., with zero velocity. The two particle trajectories are very similar, which indicates the independence of the results on the particle initial conditions. Although the initial particle velocity does not affect the trajectory of the particle radial position, it influences the motion in the cross section of the pipe, as reported in Fig. 6(c). Indeed, only the latter case exhibits a straight radial motion from the particle initial position towards the pipe center, while in the former case a nonzero azimuthal velocity is observed. As already mentioned, please note that we have also verified that this behavior is independent of the grid resolution used.

The trajectories of the particles in the y-z plane from their initial position until the final equilibrium are depicted in Fig. 7 for all the Reynolds, Re, and Weber, We, numbers considered. The initial and final equilibrium positions of the particles are marked with black squares and purple circles in the figure. Clearly, the results show that independently of the Reynolds numbers Re under investigation, the particle path length decreases with the Weber number We. Indeed, for the highest We considered [Fig. 7(c)], the particle moves straight inward toward the center of the pipe along

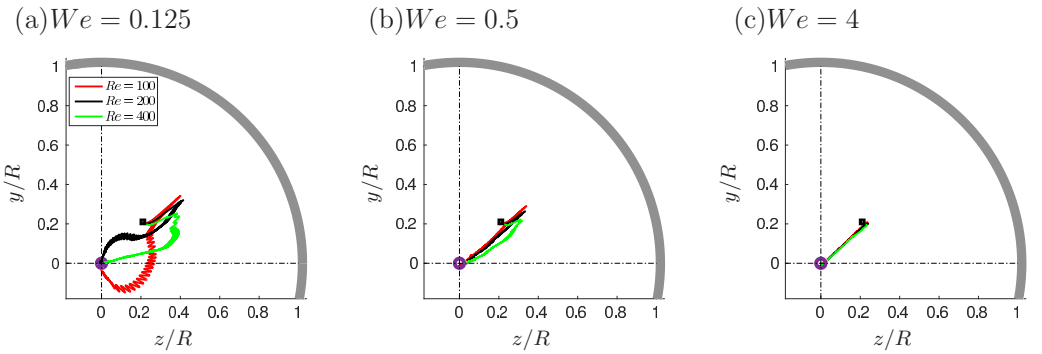

FIG. 7. Trajectory of the particle in the pipe cross section (y-z plane) at different Reynolds numbers Re and for various Weber numbers We. The black squares and purple circles show the initial and the final equilibrium positions, respectively.

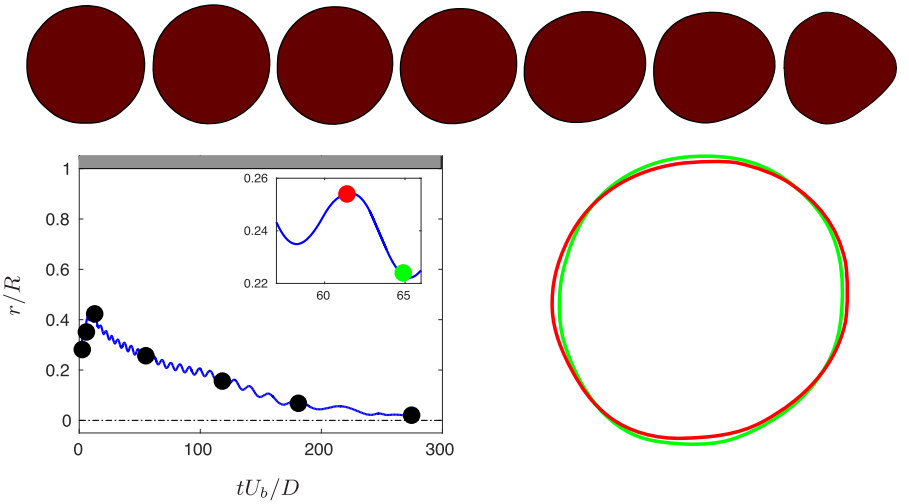

FIG. 8. Cross section of the deformed shape of an hyperelastic particle at Re = 200 and We = 0.5 at seven different time instants, marked in the time history of the radial position with black circles, from the initial to the equilibrium position. The red and green lines represent the change of particle shape during an oscillation.

the radial direction, with all the trajectories for different Reynolds number Re collapsing into a single line. On the other hand, as the Weber number decreases and the particle rigidity increases, the motion becomes more complex, with the particle initially moving toward the pipe walls, and then shooting back toward the center of the pipe. Moreover, as the Weber number decreases, we can observe that particles at different Reynolds numbers exhibit different cross-sectional trajectories, as clearly shown in Fig. 7(a).

During the migration, the particle deforms and changes shape due to the different hydrodynamic stresses imposed by the flow at the different radial positions, as depicted in Fig. 8. In particular, we observe that the particle, initially spherical, deforms into an asymmetric shape during its migration motion and finally assumes an axial-symmetric configuration when reaching the center of the channel. Indeed, the particle asymmetric shape and the related nonuniform mean velocity profile are crucial for the particle migration process [10]. This is detailed in Fig. 8, where we display the shapes assumed by the particle during their motion for the case with Re = 200 and We = 0.5; the leftmost panel represents the particle initial shape (at time $t = 0$), the rightmost panel the particle final shape at the equilibrium (at time $t = t_{\mathrm{cen}}$), while the middle panels the shape assumed during the migration. In the first part of the process ($t \lesssim 5D/U_b$), the shape is approximately spherical, and the particle migrates toward the wall; when the deformation builds up and the particle becomes asymmetric, the particle reverts its motion and displaces toward the pipe centerline. As already stated above, this transient shape is nonsymmetric due to the different shear rates at various wall-normal distances and the finite size of the particle. On the other hand, the particle assumes an axial-symmetric bullet-like shape when it reaches the pipe center due to the symmetry of the velocity profile. Similar shapes were observed both numerically and experimentally by various authors in the past for deformable vesicles, particles, capsules, and cells [10,30,60–63], in the limit of vanishing Reynolds numbers, as this corresponds to a minimum of the elastic energy. Figure 8 also shows how the particle shape changes during its oscillatory motion. In particular, the figure reports the particle shape over half a period of osicllation, i.e., $T_{\mathrm{osc}}/2$. As expected, we observe that the particle shape slightly changes during the oscillation process; however, the amplitude of the oscillation is small, around 1% of R.

In Fig. 9, we show the effect of the Reynolds and Weber numbers on the equilibrium shape of the particle. From the figures, we note that the equilibrium shape of the particle is only slightly affected by variations of the Reynolds number Re (top row in Fig. 9), while the shape changes with

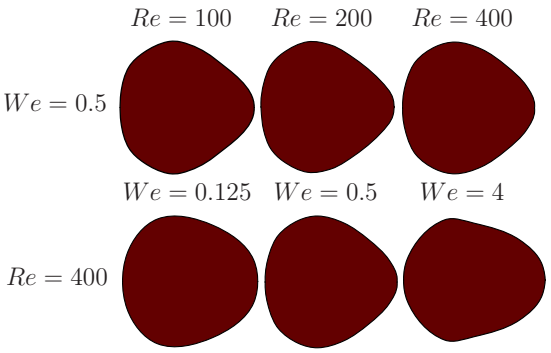

FIG. 9. Cross section of the deformed shape of an hyperelastic particle for (top) three different Reynolds numbers and at the same Weber number We = 0.5 and for (bottom) three different Weber numbers and at the same Reynolds number Re = 400 at the final equilibrium state.

the Weber number (bottom row in Fig. 9); in particular, at high Weber numbers We, the particle becomes more elongated than for low We. These results are consistent with what was previously observed in Figs. 2 and 3.

Next, we discuss the forces acting on the particle to explain its migration dynamics. In the case of a neutrally buoyant rigid particle suspended in a Newtonian fluid, the particle migration and final equilibrium position are determined by two opposing forces acting on the particle: These forces are the wall-induced lift force that pushes the particle away from the wall and the shear-gradient-induced lift force that drives the particle toward the wall, the latter resulting from the rigid particle resistance to deformation [16,28]. When the particle is deformable, its dynamics is further complicated by the additional force originating from the particle shape deformation, which depends on the elastic properties of the material (e.g., the elastic modulus G) [30,31]. Note that the particle deformation also affects and modifies the other two forces.

Figures 10(a)–10(c) shows the total force acting on the particle for different Reynolds numbers and for various Weber numbers, as a function of time. We observe that the total force is positive at the beginning of the simulation, then changes sign, and finally vanishes to zero at later times. This is consistent with what observed in Fig. 2, which shows that the particle first moves toward the walls and then changes direction to move toward the center. This behavior is due to the fact that the particle is initially spherical and thus tends to focus around $0.6R$, but then starts deforming and the asymmetric shape drives the particle to the centerline; this is not an instantaneous process due to the finite inertia of the flow and the elastic timescale. In particular, the migration timescale mostly changes with the Weber number, as shown in the figure: For small We (low deformability)

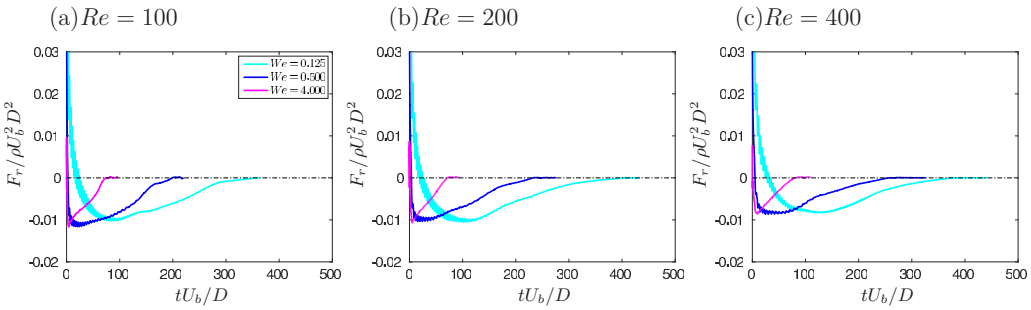

FIG. 10. The time history of the normalized total radial forces F_r acting on the particle at different Reynolds numbers Re and for various Weber numbers We.

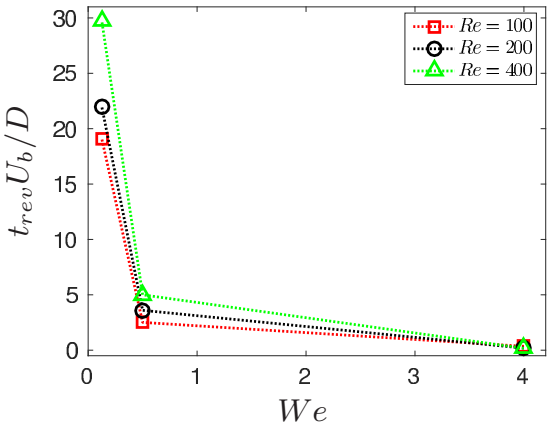

FIG. 11. Normalized time needed to reverse the sign of the total force acting on the particle, t_{rev}, vs the Weber number We for different Re.

the process is slow, while for high We (high deformabilty) the process is fast. We conjecture that, for $\text{We} = 0$ (rigid particle), the process needs an infinite time and thus would never happen, leading to the particle focusing at $0.6R$; indeed, we can observe in Fig. 4(b) that the time needed to focus at the centerline strongly increases when reducing the Weber number, apparently diverging for $\text{We} = 0$. This is also shown in Fig. 11 where the time t_{rev} when the total force is first null, $F_r = 0$ (i.e. it changes sign), is reported as a function of the Weber number We and for different Reynolds numbers Re. As observed for the focusing time in Fig. 4(b), t_{rev} decreases with the Weber number and only slightly increases with the Reynolds number. The growth of t_{rev} with the Reynolds number is due to the increase of the particle inertia, which requires longer times to invert its motion. Also, t_{rev} tends to zero for $\text{We} \to \infty$ and tends to infinity for $\text{We} \to 0$.

Finally, we compute the average over the particle volume of each term appearing in the momentum conservation equation, i.e., the pressure, nonlinear inertial, viscous, and elastic contributions to Eq. (1c); in particular, the force components in the ith direction are computed as

$$F_i^P = -\int_{\mathcal{V}^s} \frac{\partial P}{\partial x_i}\, d\mathcal{V}, \quad F_i^I = -\int_{\mathcal{V}^s} \frac{\partial u_i^s u_j^s}{\partial x_j}\, d\mathcal{V},$$
$$F_i^V = \int_{\mathcal{V}^s} \mu^s \frac{\partial}{\partial x_j}\left(\frac{\partial u_i^s}{\partial x_j} + \frac{\partial u_j^s}{\partial x_i}\right) d\mathcal{V}, \quad F_i^E = \int_{\mathcal{V}^s} G\frac{\partial \xi_{ij}}{\partial x_j}\, d\mathcal{V}. \tag{10}$$

Note that the sum with sign of these terms gives the rate of change of the particle velocity; also, by applying Gauss's theorem, we can rewrite F_i^P and F_i^V as surface integrals, as in the classical definitions of pressure and viscous contributions to the lift and drag forces on an object. For a completely solid particle, the force balance is given by the wall-induced lift force (F_i^P) arising from the interaction of the particle and the neighboring wall pushing toward the channel centerline, and a shear gradient lift force pulling the particle toward the wall. The latter arises from the fact that the particle, being rigid, cannot sustain the torque generated by the mean shear gradient (F_i^V and F_i^I) and thus starts to rotate. In the case of a deformable particle, one additional force is present (F_i^E): the elastic force inside the particle. Figure 12 shows these different terms for the case with $\text{Re} = 200$ and different We; first, we observe that the viscous force is approximately zero and does not contribute to the momentum balance, which is due to the fact that the particle can actually deform. From the figure, we can also infer that the pressure term is negative, similar to the rigid particle case, thus pushing the particle toward the centerline, while the elastic and nonlinear terms are positive, thus pushing the particle toward the wall. In the initial part of the particle dynamics,

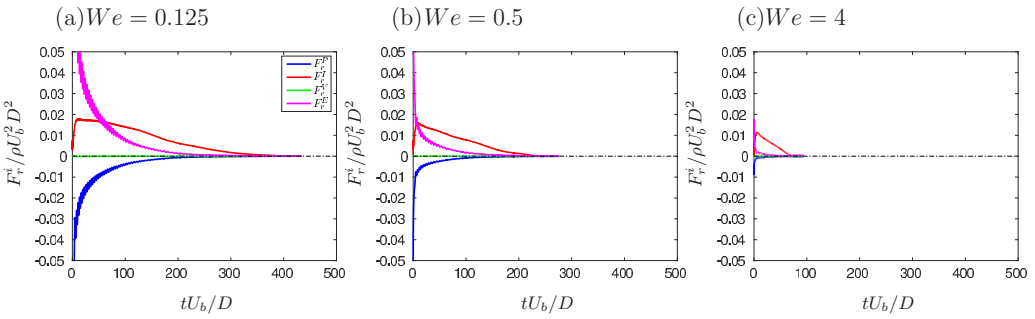

FIG. 12. The time history of the normalized radial force components F_r^i acting on the particle for different Weber numbers and a fixed Reynolds number Re $= 200$.

the nonlinear term is zero and slowly grows, while the two dominant force contributions are the pressure and elastic forces, the latter being the largest, so that, overall, these induce the movement of the particle toward the wall. As the particle deforms and aligns with the mean shear, the elastic force decreases rapidly, and the nonlinear term becomes the dominant one. However, deformation also prevents particle rotation, thus significantly reducing the inertial force toward the wall. As a consequence, there remains only a pressure-induced force toward the center. As the deformation is faster for larger values of the Weber number, the lateral migration velocity increases with We, i.e., the focusing time decreases with deformability. From Fig. 12 we observe that, not only the total force is null when the particle reaches the centerline, but also all the force components vanish due to the symmetry; this is very different from the Segrè-Silberberg equilibrium position where the total force is zero, but the single-force components are not. This discussion holds for all the Weber numbers considered in this study; however, as We increases, the time needed to reach the equilibrium strongly reduces, consistent with the fact that for We $= 0$ this time should go to infinity.

Finally, in this last section, we briefly assess the effect of the ratio of the solid viscosity μ^s to the fluid viscosity μ^f. Here, we focus our analysis on a single Reynolds number Re $= 400$ and Weber number We $= 4$, and we consider three different values of the solid viscosity ratio, covering one order of magnitude: $\mu^s = 0.3$, 1, and $3\mu^f$. Figure 13 reports the time history of the particle radial position; in general, the results suggest that high solid viscosity makes the particle effectively more

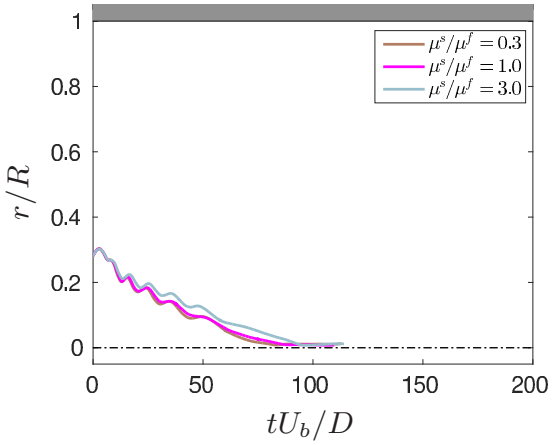

FIG. 13. Time history of the radial position of the deformable particle for three different solid/fluid viscosity ratios at the same Reynolds and Weber numbers: Re $= 400$ and We $= 4$.

rigid, thus exhibiting a behavior more similar to that of stiffer particles; i.e., the time needed to reach the equilibrium position in the channel centerline increases with μ^s. Conversely, low values of μ^s increase the particle deformation, thus reducing the time t_{cen} needed to reach the final equilibrium position. Note that the particle trajectory is only weakly modified by this parameter (compared to the modification induced by We), at least for the range of parameters considered in this work. These results are in agreement with what previously observed by Rosti and Brandt in Ref. [56].

IV. CONCLUSIONS AND FINAL REMARKS

We study the dynamics of an hyperelastic neo-Hookean deformable particle suspended in a Newtonian fluid in a straight pipe with circular cross section. Different finite Reynolds and Weber numbers are considered, in order to evaluate the effects of inertia and elasticity on the particle focusing. The problem is studied numerically through an extensively validated fully Eulerian formulation based on the one-fluid formulation where a single set of equations is solved for both the fluid and solid phases.

We find that the particle deforms and undergoes a lateral displacement while traveling downstream through the pipe, always focusing at the pipe centerline. While the particle final equilibrium position is independent of the Reynolds and Weber numbers considered, its migration dynamics strongly depends on the particle elasticity while it is only slightly affected by the Reynolds number. In particular, the migration is faster as the elasticity increases, with the particle reaching the final equilibrium position at the centerline in shorter times when more deformable.

When the particle is injected in the flow at some intermediate position, it first moves toward the walls, aiming for the famous Segrè-Silberberg equilibrium position of rigid particles ($0.6R$). However, as soon as the particle starts deforming, it changes direction of motion and starts migrating toward the centerline. Indeed, the particle, initially spherical, deforms into an asymmetric shape due the nonuniform shear, which ultimately causes its movement to the centerline. Indeed, when the final equilibrium position at the pipe center is reached, the particle assumes an axisymmetric bulletlike shape that enforces the equilibrium.

In order to explain the migration dynamics, we analyze the force acting on the particle and found that the total force is first positive, thus pushing the particle toward the wall, then becomes negative, causing the particle migration to the centerline, and finally vanishes to zero when the particle reaches the final equilibrium position. We decompose the total force acting on the particle in different contributions, i.e., the viscous, pressure, inertial, and elastic contributions. We found that the viscous force is negligible, the pressure term is responsible for pushing the particle toward the centerline, similar to the rigid particle case, while the elastic and inertial ones are opposing the movement and trying to pull the particle toward the wall. However, this opposition is only limited to the initial transient phase, as particle deformation aligns it with the local shear, reducing the elastic force, and, more important, prevents particle rotation, which quenches the inertial force towards the wall. Indeed, the migration is faster, when the deformation is faster, i.e., for larger values of the Weber number.

Finally, we show the effect of the solid to fluid viscosity ratio and show that high solid viscosity makes the particle effectively more rigid, so that it requires a longer time to reach the equilibrium position when compared to cases with low values of solid viscosity. Also, we observe that the effect of the solid viscosity is smaller than that of the Weber number.

ACKNOWLEDGMENTS

The authors were supported by the European Research Council Grant No. ERC-2013-CoG-616186, TRITOS, and by the Swedish Research Council Grant No. VR 2014-5001. The authors acknowledge computer time provided by the Swedish National Infrastructure for Computing (SNIC). Dhiya Alghalibi would like to gratefully acknowledge his graduate scholarship from the Iraqi Ministry of Higher Education and Scientific Research via University of Kufa.

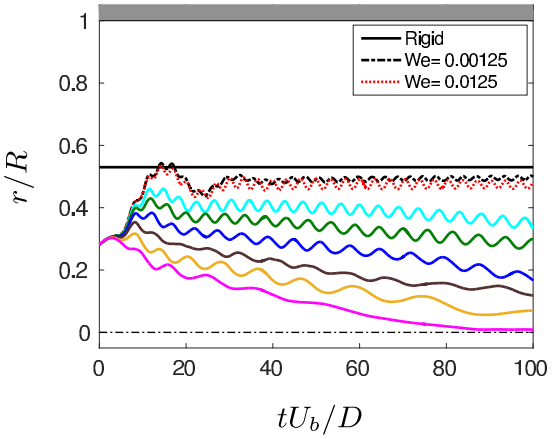

FIG. 14. The time history of the particle radial position r at different Weber numbers We at constant Reynolds numbers $\mathrm{Re} = 400$, as indicated in the legend. The radial position r is normalized by the radius of the pipe R whereas time is scaled by D/U_b.

APPENDIX: THE RIGID PARTICLE LIMIT

All the cases studied in the rest of the paper show that the final equilibrium position of a deformable particle is the centerline and that the time needed to go toward the center grows as the particle becomes more rigid. Here, we show some additional results for very rigid particles (high modulus of transverse elasticity G) to enforce this concept and to show that the limit of fully rigid particle can be approached and the Segrè-Silberberg equilibrium position recovered. Figure 14 displays the results for a particle at $\mathrm{Re} = 400$ and all the We considered in the study plus two additional cases with very rigid particles (yet not fully rigid). As shown in the figure, the equilibrium position approaches the value predicted for a fully rigid particle as G increases, tending to the value $0.53R$ predicted by Asmolov [19] for a finite-size rigid particle as the one considered here. Although in the chosen time frame the most rigid particle does not move toward the centerline yet, it will eventually deform and will start moving toward it. This process takes place in a time which strongly grows with G, as also shown in the main text of this paper. Thus, we can consider a perfectly rigid particle as a deformable one with infinite modulus of transverse elasticity that requires an infinite time to deform and start displacing toward the channel centerline.

[1] N. Pamme, Continuous flow separations in microfluidic devices, Lab Chip **7**, 1644 (2007).
[2] A. Karimi, S. Yazdi, and A. M. Ardekani, Hydrodynamic mechanisms of cell and particle trapping in microfluidics, Biomicrofluidics **7**, 021501 (2013).
[3] H. Lim, J. Nam, and S. Shin, Lateral migration of particles suspended in viscoelastic fluids in a microchannel flow, Microfluid. Nanofluidics **17**, 683 (2014).
[4] D. A. Ateya, J. S. Erickson, P. B. Howell, L. R. Hilliard, J. P. Golden, and F. S. Ligler, The good, the bad, and the tiny: A review of microflow cytometry, Anal. Bioanal. Chem. **391**, 1485 (2008).
[5] X. Xuan, J. Zhu, and C. Church, Particle focusing in microfluidic devices, Microfluidics and nanofluidics **9**, 1 (2010).
[6] K. Kang, S. S. Lee, K. Hyun, S. J. Lee, and J. M. Kim, DNA-based highly tunable particle focuser, Nat. Commun. **4**, 2567 (2013).
[7] G. Li, G. H. McKinley, and A. M. Ardekani, Dynamics of particle migration in channel flow of viscoelastic fluids, J. Fluid Mech. **785**, 486 (2015).

[8] X. Lu, C. Liu, G. Hu, and X. Xuan, Particle manipulations in non-Newtonian microfluidics: A review, J. Colloid Interface Sci. **500**, 182 (2017).
[9] E. Guazzelli and J. F. Morris, *A Physical Introduction to Suspension Dynamics*, Cambridge Text in Applied Mathematics Vol. 45 (Cambridge University Press, Cambridge, UK, 2011).
[10] B. Kaoui, G. H. Ristow, I. Cantat, C. Misbah, and W. Zimmermann, Lateral migration of a two-dimensional vesicle in unbounded Poiseuille flow, Phys. Rev. E **77**, 021903 (2008).
[11] F. Risso, F. Collé-Paillot, and M. Zagzoule, Experimental investigation of a bioartificial capsule flowing in a narrow tube, J. Fluid Mech. **547**, 149 (2006).
[12] P. Bagchi, Mesoscale simulation of blood flow in small vessels, Biophys. J. **92**, 1858 (2007).
[13] G. Coupier, B. Kaoui, T. Podgorski, and C. Misbah, Noninertial lateral migration of vesicles in bounded Poiseuille flow, Phys. Fluids **20**, 111702 (2008).
[14] G. R. Lázaro, A. Hernández-Machado, and I. Pagonabarraga, Rheology of red blood cells under flow in highly confined microchannels. II. Effect of focusing and confinement, Soft Matter **10**, 7207 (2014).
[15] C. Bächer, L. Schrack, and S. Gekle, Clustering of microscopic particles in constricted blood flow, Phys. Rev. Fluids **2**, 013102 (2017).
[16] D. Stoecklein and D. Di Carlo, Nonlinear microfluidics, Anal. Chem. **91**, 296 (2018).
[17] G. Segre and A. Silberberg, Radial particle displacements in Poiseuille flow of suspensions, Nature (London) **189**, 209 (1961).
[18] J. A. Schonberg and E. J. Hinch, Inertial migration of a sphere in Poiseuille flow, J. Fluid Mech. **203**, 517 (1989).
[19] E. S. Asmolov, The inertial lift on a spherical particle in a plane Poiseuille flow at large channel Reynolds number, J. Fluid Mech. **381**, 63 (1999).
[20] J. Feng, H. H. Hu, and D. D. Joseph, Direct simulation of initial value problems for the motion of solid bodies in a Newtonian fluid. Part 2. Couette and Poiseuille flows, J. Fluid Mech. **277**, 271 (1994).
[21] B. H. Yang, J. Wang, D. D. Joseph, H. H. Hu, T.-W. Pan, and R. Glowinski, Migration of a sphere in tube flow, J. Fluid Mech. **540**, 109 (2005).
[22] A. Karnis, H. L. Goldsmith, and S. G. Mason, The flow of suspensions through tubes: V. Inertial effects, Can. J. Chem. Eng. **44**, 181 (1966).
[23] J.-P. Matas, J. F. Morris, and É. Guazzelli, Inertial migration of rigid spherical particles in Poiseuille flow, J. Fluid Mech. **515**, 171 (2004).
[24] D. Di Carlo, D. Irimia, R. G. Tompkins, and M. Toner, Continuous inertial focusing, ordering, and separation of particles in microchannels, Proc. Nat. Acad. Sci. USA **104**, 18892 (2007).
[25] D. Di Carlo, Inertial microfluidics, Lab Chip **9**, 3038 (2009).
[26] Y.-S. Choi, K.-W. Seo, and S.-J. Lee, Lateral and cross-lateral focusing of spherical particles in a square microchannel, Lab Chip **11**, 460 (2011).
[27] B. P. Ho and L. G. Leal, Inertial migration of rigid spheres in two-dimensional unidirectional flows, J. Fluid Mech. **65**, 365 (1974).
[28] J. M. Martel and M. Toner, Inertial focusing in microfluidics, Annu. Rev. Biomed. Eng. **16**, 371 (2014).
[29] I. Lashgari, M. N. Ardekani, I. Banerjee, A. Russom, and L. Brandt, Inertial migration of spherical and oblate particles in straight ducts, J. Fluid Mech. **819**, 540 (2017).
[30] A. H. Raffiee, S. Dabiri, and A. M. Ardekani, Elasto-inertial migration of deformable capsules in a microchannel, Biomicrofluidics **11**, 064113 (2017).
[31] P. Hadikhani, S. Mohammad H. Hashemi, G. Balestra, L. Zhu, M. A. Modestino, F. Gallaire, and D. Psaltis, Inertial manipulation of bubbles in rectangular microfluidic channels, Lab Chip **18**, 1035 (2018).
[32] S. K. Doddi and P. Bagchi, Lateral migration of a capsule in a plane Poiseuille flow in a channel, Int. J. Multiphase Flow **34**, 966 (2008).
[33] D. Salac and M. J. Miksis, Reynolds number effects on lipid vesicles, J. Fluid Mech. **711**, 122 (2012).
[34] L. Zhu, C. Rorai, D. Mitra, and L. Brandt, A microfluidic device to sort capsules by deformability: A numerical study, Soft Matter **10**, 7705 (2014).
[35] B. Kim, C. B. Chang, S. G. Park, and H. J. Sung, Inertial migration of a 3d elastic capsule in a plane Poiseuille flow, Int. J. Heat Fluid Flow **54**, 87 (2015).

[36] Z. Wang, Y. Sui, A.-V. Salsac, D. Barthès-Biesel, and W. Wang, Motion of a spherical capsule in branched tube flow with finite inertia, J. Fluid Mech. **806**, 603 (2016).
[37] A. J. Mach and D. Di Carlo, Continuous scalable blood filtration device using inertial microfluidics, Biotechnol. Bioeng. **107**, 302 (2010).
[38] S. C. Hur, N. K. Henderson-MacLennan, E. R. B. McCabe, and D. Di Carlo, Deformability-based cell classification and enrichment using inertial microfluidics, Lab Chip **11**, 912 (2011).
[39] A. Kilimnik, W. Mao, and A. Alexeev, Inertial migration of deformable capsules in channel flow, Phys. Fluids **23**, 123302 (2011).
[40] Y.-L. Chen, Inertia- and deformation-driven migration of a soft particle in confined shear and Poiseuille flow, RSC Adv. **4**, 17908 (2014).
[41] S. J. Shin and H. J. Sung, Inertial migration of an elastic capsule in a Poiseuille flow, Phys. Rev. E **83**, 046321 (2011).
[42] T. Krüger, B. Kaoui, and J. Harting, Interplay of inertia and deformability on rheological properties of a suspension of capsules, J. Fluid Mech. **751**, 725 (2014).
[43] A. M. Leshansky, A. Bransky, N. Korin, and U. Dinnar, Tunable Nonlinear Viscoelastic "Focusing" in a Microfluidic Device, Phys. Rev. Lett. **98**, 234501 (2007).
[44] S. Yang, J. Y. Kim, S. J. Lee, S. S. Lee, and J. M. Kim, Sheathless elasto-inertial particle focusing and continuous separation in a straight rectangular microchannel, Lab Chip **11**, 266 (2011).
[45] M. K. S. Verma and V. Kumaran, A multifold reduction in the transition Reynolds number, and ultra-fast mixing, in a micro-channel due to a dynamical instability induced by a soft wall, J. Fluid Mech. **727**, 407 (2013).
[46] J. Bonet and R. D. Wood, *Nonlinear Continuum Mechanics for Finite Element Analysis* (Cambridge University Press, Cambridge, UK, 1997).
[47] G. Tryggvason, M. Sussman, and M. Y. Hussaini, Immersed boundary methods for fluid interfaces, Comp. Methods Multiphase Flow **3**, 37 (2007).
[48] M. Quintard and S. Whitaker, Transport in ordered and disordered porous media II: Generalized volume averaging, Transp. Porous Media **14**, 179 (1994).
[49] S. Takeuchi, Y. Yuki, A. Ueyama, and T. Kajishima, A conservative momentum-exchange algorithm for interaction problem between fluid and deformable particles, Int. J. Numer. Methods Fluids **64**, 1084 (2010).
[50] K. Sugiyama, S. Ii, S. Takeuchi, S. Takagi, and Y. Matsumoto, A full Eulerian finite difference approach for solving fluid-structure coupling problems, J. Comput. Phys. **230**, 596 (2011).
[51] J. Kim and P. Moin, Application of a fractional-step method to incompressible Navier-Stokes equations, J. Comput. Phys. **59**, 308 (1985).
[52] T. Min, J. Y. Yoo, and H. Choi, Effect of spatial discretization schemes on numerical solutions of viscoelastic fluid flows, J. Non-Newtonian Fluid Mech. **100**, 27 (2001).
[53] C.-W. Shu, High order weighted essentially nonoscillatory schemes for convection dominated problems, SIAM Rev. **51**, 82 (2009).
[54] A. Shahmardi, S. Zade, M. Ardekani, R. J. Poole, F. Lundell, M. E. Rosti and L. Brandt, Turbulent duct flow with polymers, J. Fluid Mech. **859**, 1057 (2019).
[55] M. E. Rosti and L. Brandt, Numerical simulation of turbulent channel flow over a viscous hyper-elastic wall, J. Fluid Mech. **830**, 708 (2017).
[56] M. E. Rosti and L. Brandt, Suspensions of deformable particles in a Couette flow, J. Non-Newtonian Fluid Mech. **262**, 3 (2018).
[57] M. E. Rosti, L. Brandt, and D. Mitra, Rheology of suspensions of viscoelastic spheres: Deformability as an effective volume fraction, Phys. Rev. Fluids **3**, 012301 (2018).
[58] B. Kadoch, D. Kolomenskiy, P. Angot, and K. Schneider, A volume penalization method for incompressible flows and scalar advection-diffusion with moving obstacles, J. Comput. Phys. **231**, 4365 (2012).
[59] H. Amini, W. Lee, and D. Di Carlo, Inertial microfluidic physics, Lab Chip **14**, 2739 (2014).
[60] M. M. Villone, F. Greco, M. A. Hulsen, and P. L. Maffettone, Numerical simulations of deformable particle lateral migration in tube flow of Newtonian and viscoelastic media, J. Non-Newtonian Fluid Mech. **234**, 105 (2016).

[61] V. Vitkova, M. Mader, and T. Podgorski, Deformation of vesicles flowing through capillaries, EPL **68**, 398 (2004).

[62] C. Schaaf and H. Stark, Inertial migration and axial control of deformable capsules, Soft Matter **13**, 3544 (2017).

[63] M. Mokbel, D. Mokbel, A. Mietke, N. Traber, S. Girardo, O. Otto, J. Guck, and S. Aland, Numerical simulation of real-time deformability cytometry to extract cell mechanical properties, ACS Biomater. Sci. Eng. **3**, 2962 (2017).